

## Article

# Large Signal Stability Criteria Combined with a 3D Region of Asymptotic Stability Method for Islanded AC/DC Hybrid Microgrids

Xinbo Liu , Zhenkang Zhu, Junfu Shi, Xiaotong Song and Jinghua Zhou

School of Electrical and Control Engineering, North China University of Technology, Beijing 100144, China

\* Correspondence: liuxinbo@ncut.edu.cn

**Abstract:** Large disturbances frequently happen in isolated AC/DC Hybrid Microgrids. Unfortunately, constant power loads (CPLs) with negative impedance characteristics are equivalent to positive feedback, resulting in an increase in large disturbances. The system can easily become unstable. Consequently, large signal stability criteria are proposed in this paper. Combined with a three-dimensional region of asymptotic stability (3D RAS) method for islanded AC/DC Hybrid Microgrids, important parameters to increase stability margins were determined. Firstly, mixed potential theory was used to derive a large-signal stability criterion. The criteria gave constraints on filtering parameters, CPL power, power of the battery to charge and discharge, AC resistive loads, and DC bus voltage. Then, Lyapunov functions were constructed, and the Lasalle invariance principle was adopted to achieve 3D RAS. When large disturbances emerged, and simultaneously voltage and current varied in 3D RAS, the system always obtained stability and reached new steady-state equilibrium points. Finally, according to comparisons, bigger capacitances of the DC bus capacitor and the AC capacitor, larger battery discharging power and smaller charging power could significantly increase stability margins of islanded Microgrids. Simulations and experimental data have shown that the large signal stability criteria and the 3D RAS work.

**Keywords:** AC/DC hybrid microgrid; constant power loads (CPLs); 3D region of asymptotic stability (3D RAS); large signal stability



**Citation:** Liu, X.; Zhu, Z.; Shi, J.; Song, X.; Zhou, J. Large Signal Stability Criteria Combined with a 3D Region of Asymptotic Stability Method for Islanded AC/DC Hybrid Microgrids. *Electronics* **2022**, *11*, 4042. <https://doi.org/10.3390/electronics11234042>

Academic Editor: Jahangir Hossain

Received: 29 October 2022

Accepted: 29 November 2022

Published: 5 December 2022

**Publisher's Note:** MDPI stays neutral with regard to jurisdictional claims in published maps and institutional affiliations.



**Copyright:** © 2022 by the authors. Licensee MDPI, Basel, Switzerland. This article is an open access article distributed under the terms and conditions of the Creative Commons Attribution (CC BY) license (<https://creativecommons.org/licenses/by/4.0/>).

## 1. Introduction

With declining fossil energy production, the energy crisis has led to the widespread use of solar PV and wind power [1]. Microgrids consist of distributed renewable energy sources, controllable loads, energy storage devices and various converters [2–5]. AC/DC Hybrid Microgrids possess DC and AC busbars, combining the advantages of both AC and DC Microgrids [6,7]. In islanded AC/DC Hybrid Microgrids, energy storage unit balances the generation power and consumption power, and stable operations are easily maintained without large disturbances [8–10]. Unfortunately, due to the high proportion of power electronic equipment and their low inertia, system sensitivity to significant disturbances is high in islanded AC/DC Hybrid Microgrids, and it is quite difficult to obtain large signal stability [11].

Furthermore, in islanded AC/DC Hybrid Microgrids, on account of their closed-loop control connection to the bus, the majority of loads are considered to be CPLs with negative incremental impedance characteristics [12]. CPLs are equivalent to positive feedback during large disturbances and easily introduce instability [13–15]. Consequently, guaranteeing the stability of islanded Hybrid Microgrids with CPLs during large disturbances has become an essential issue.

A lot of methods have been proposed to conduct large signal stability analysis [16–18]. In reference [19], Lyapunov's theorem has been used to create an adaptive disturbance

estimator to reduce external disturbances and parameter uncertainty. In [20], the Lyapunov function of the DC power system is derived using the BDQLF method and the Takagi–Sugeno model, and the stability of the system is investigated. Reference [21] considers converter structure changes, established a nonlinear reduced-order model, analyzes large signal stability, and reveals an instability mechanism. To ensure system stability during a large disturbance, Ref. [22] proposes a mixed-potential-theory-based stability criteria. In [14,23], mixed potential function(MPF) is used to derive a DC Microgrid's large signal stability requirement and interpret the relationship between system parameters and stability. The voltage frequency and current control mechanisms of isolated microgrids that are fed by controlled inverters are investigated in [24], and the large signal stability of the system was investigated. In [25], the research object is the AC/DC hybrid microgrid, with a particular focus on developing the Liapunov function and analyzing the system's large signal stability. Although the system's large signal stability criteria are derived from the aforementioned literature, the region of asymptotic stability (RAS) and stability margins were regrettably not stated.

A nonlinear DC grid's stability analysis of each equilibrium point and convergence analysis of state trajectories are both accomplished in [26], which suggests a large signal stability investigation of the standpoints of potential theory. In [27], a large signal stability method for the VSC-HVDC system based on attraction domain estimation is proposed, and the large signal stability of the VSC-HVDC system is analyzed. In [28], the large signal stability of DCMG is proposed, the influences of circuit parameters, power flow and topology changes on stability is revealed, and finally, RAS is estimated. References [26–28] investigate the stability domain of a DC system built from paralleled DC/DC converters. For an AC/DC Hybrid system, [29] estimates the RAS of the system, and discusses parameter influences on RAS. Reference [30] establishes a large signal nonlinear model and derives RAS of AC Microgrids, and influences of load transients and voltage source changes on RASs are proposed. In [31], the Liapunov functions and their RAS have been made for generators and power sharing loads in the microgrid. According to [32], the load level can have a substantial impact on the amplitude of the RAS in a DC power system. References [29–32] obtained a relatively simple two-dimensional RAS (2D RAS) for a AC/DC Hybrid Microgrids system, and the stability domain studied generally involves only two state variables in the Microgrids, which cannot describe the stability domain of the whole Microgrid system in more detail.

Moreover, mixed potential function(MPF) derives stability criterion in analytic form, and is more suitable for large signal stability analysis of nonlinear system [33,34]. MPF is usually adopted for AC/DC hybrid Microgrid analysis, and obtain a relatively simple two-dimensional RAS (2D RAS). However, only two state variables are considered and more details of the system are neglected.

RAS is quite important to quantitatively indicate the parameter influences on system stability margins. In fact, actual Microgrids are extremely complicated, and more than two state variables (capacitor voltages and/or inductor currents) are usually involved. Unfortunately, existing stability analysis methods obtain 2D RAS only related to two state variables for simple systems. Consequently, deriving the RAS of more state variables for complicated systems has attracted a lot of attention. In particular, how to propose 3D RAS related to three state variables for islanded AC/DC Hybrid Microgrids has become a key issue.

The mixed potential function can establish Liapunov-type energy functions and also achieve large signal stability criteria. It is more appropriate for large-signal stability analysis, notably in regard to instability problems induced by constant power loads [33,34]. Consequently, the mixed potential function is used in this paper to establish large signal stability criteria and the Lyapunov function model, and then the Lasalle invariance principle is introduced to achieve 3D RAS for islanded AC/DC Hybrid Microgrids. Furthermore, important parameters to increase stability margins are determined, especially the positive

effect of batteries as inertial links to improve system stability, and simultaneously negative effects of CPLs are also considered. The main contributions of this paper are:

- According to the coordinate transformation abc-dq, equivalent nonlinear models of islanded AC/DC Hybrid Microgrid are established.
- Based on mixed potential function, large-signal stability criteria and the Lyapunov model for islanded AC/DC Hybrid Microgrid are both derived, and the proposed criteria give constraints on filtering parameters, CPL power, power of the battery to charge and discharge, AC resistive loads, and DC bus voltage.
- On the basis of the Lyapunov model, the Lasalle invariance principle is adopted to achieve 3D RAS of islanded AC/DC Hybrid Microgrids.
- The 3D RAS indicates the larger capacitance of the DC bus capacitor and the AC capacitor; larger battery discharging power and smaller charging power could significantly increase the stability margins of islanded AC/DC Hybrid Microgrids.

## 2. System Topology and Control Strategy

The topology of AC/DC Hybrid Microgrids mainly includes a distributed generation unit, energy storage unit, DC–AC converter, constant power loads (CPLs), LC filter and AC resistive loads. The system topology is shown in Figure 1.

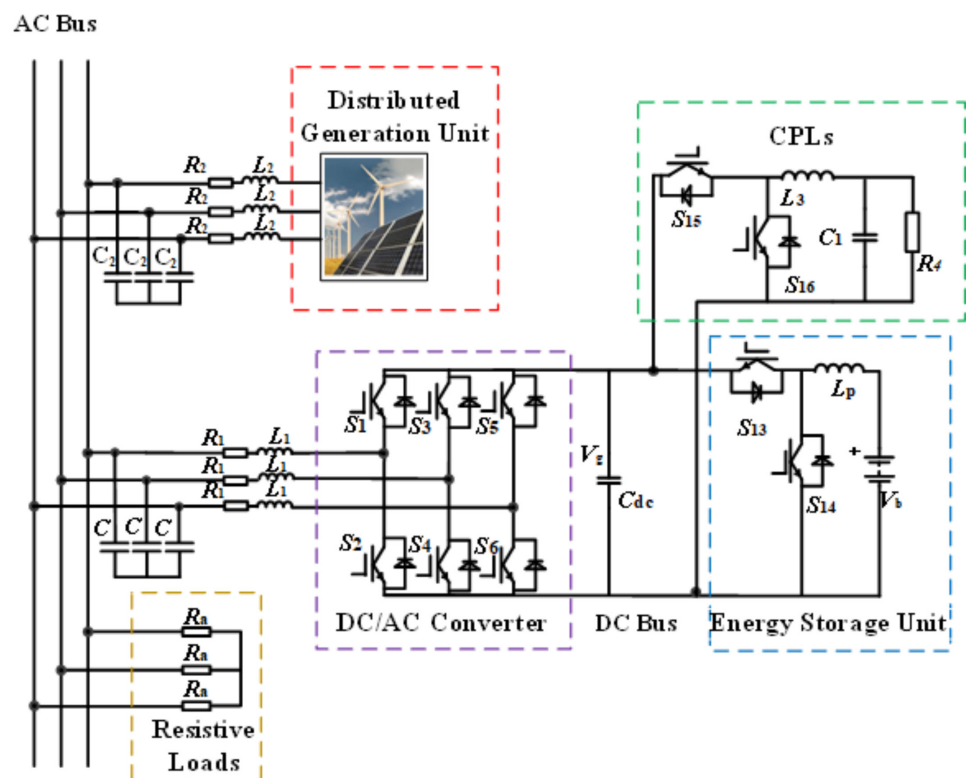


Figure 1. AC/DC Hybrid Microgrid topology.

$L_1$ ,  $R_1$  and  $C$  are filter elements of the DC–AC converter.  $V_b$  is the voltage of the batteries and  $L_3$  and  $C_1$  are filter elements of CPLs.  $R_4$  is the resistor of CPLs.  $R_a$  is the AC resistive load.  $C_{dc}$  is the DC capacitor.

The CPLs are implemented through a closed-loop controlled converter and a resistor, as shown in Figure 2. The voltage and current characteristic curve of CPLs is shown in Figure 3. As the voltage increases, the load current decreases. Consequently, it can be derived that  $\Delta v / \Delta i < 0$ , a negative incremental impedance characteristic of CPLs.

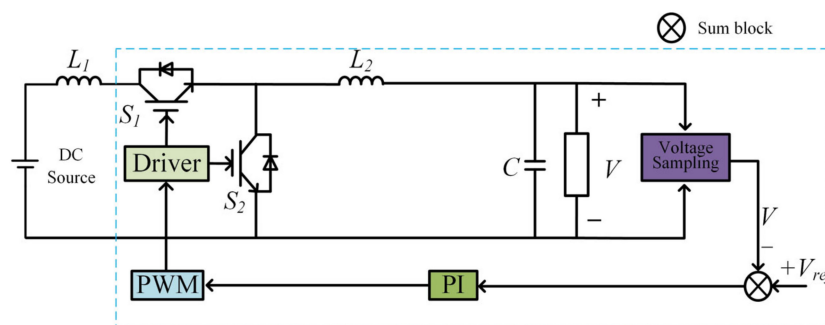


Figure 2. Representative structure of CPLs.

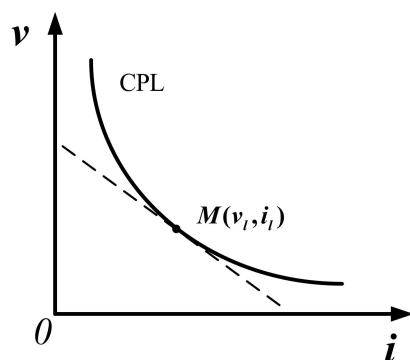


Figure 3. CPLs' voltage and current curve.

In isolated AC/DC Hybrid Microgrids, distributed generation units support the voltage and frequency of the AC bus. In the battery, the batteries are connected to the AC bus through a cascaded DC–AC converter and bidirectional DC–DC converter. The DC–DC converter adopts the DC bus voltage outer loop and inductor current inner loop, and the control block diagram is shown in Figure 4. The reference value  $v_{ref}$  of DC bus voltage is compared with the actual value  $v_{dc}$  and the output of PI voltage controller is the reference value  $i_{ref}$  of the inner loop. The output of the PI current controller is used to generate PWM charging or discharging signals. If  $v_{ref} > v_{dc}$ , that means the new energy sources are not enough to support DC bus voltage, and the discharging PWM signals are activated to increase  $v_{dc}$ . On the contrary, when  $v_{ref} < v_{dc}$ , the charging PWM signals are triggered to decrease  $v_{dc}$ .

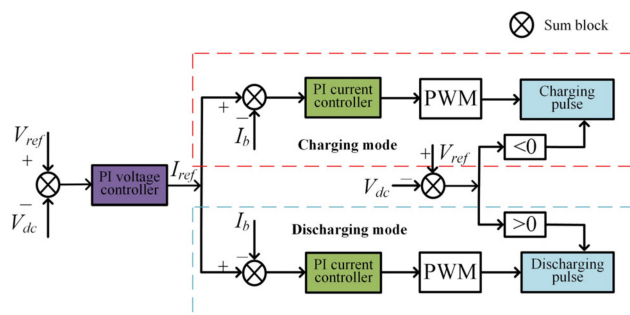


Figure 4. Bidirectional DC–DC converter control block diagram of battery.

In Figure 5,  $V_{abc}$  is three-phase voltage and  $I_{abc}$  is three-phase current.  $\theta$  is the initial phase angle obtained by PLL.  $\omega$  is angular frequency.  $u_d$  and  $u_q$  are the d-axis and q-axis components of AC voltage, respectively.  $i_d$  and  $i_q$  are the d-axis and q-axis components of AC inductor current, respectively.  $v_{dcref}$  and  $v_{dc}$  are the reference value and actual value of DC bus voltage, respectively.  $i_{dref}$  is the reference value and  $i_{qref}$  is the actual value of current inner loop.

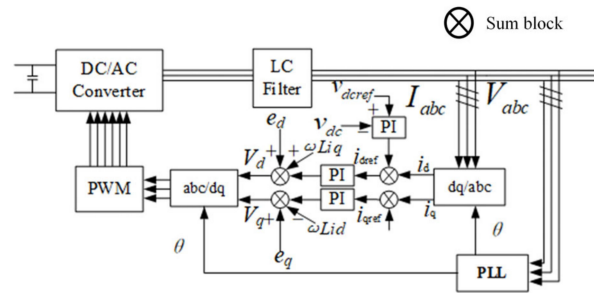


Figure 5. Bidirectional DC–AC converter control block diagram of battery.

Equivalent Nonlinear Model of Islanded AC/DC Hybrid Microgrids

To model a DC–AC converter between AC bus and DC bus, the general PWM rectifier is utilized and shown in Figure 6.  $e_a, e_b,$  and  $e_c$  are AC three-phase voltages,  $e_L$  represents DC electromotive force,  $i_a, i_b,$  and  $i_c$  are the currents through inductors,  $C_{dc}$  represents the DC capacitor,  $R_L$  is the DC load,  $L$  is the AC filter inductor,  $N$  is the DC reference point,  $v_{dc}$  represents DC bus voltage, and  $R$  is the equivalent resistance of the inductor. When  $e_L = 0$ , the DC load is pure resistor.

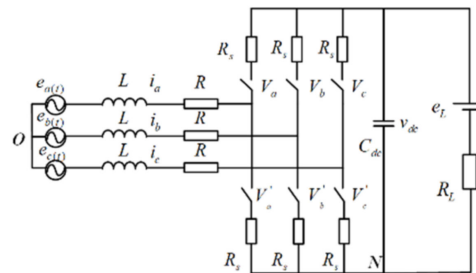


Figure 6. Topology of PWM rectifier.

Based on Figure 6, Kirchoff’s voltage equation and current equation are derived, and transformed from abc to two-phase dq, and shown as:

$$\begin{cases} L \frac{di_d}{dt} - \omega Li_q + Ri_d = e_d - v_{dc} s_d \\ L \frac{di_q}{dt} + \omega Li_d + Ri_q = e_q - v_{dc} s_q \\ C \frac{dv_{dc}}{dt} = \frac{3}{2} (i_q s_q + i_d s_d) - i_L \end{cases} \quad (1)$$

In (1),  $i_L$  is the load current, and  $i_d$  and  $i_q$  are the d-axis and q-axis components of the three-phase current. Based on the power conservation theorem and (1), the PWM rectifier is equivalent to a two-port input, single-port output, and three-port network. According to Figure 7,  $i_{dc}$  is DC current,  $v_{dc}$  is DC voltage, and  $v_d$  and  $v_q$  are the d-axis and q-axis components of the three-phase voltage, respectively.  $i_d$  and  $i_q$  are the d-axis and q-axis components of the three-phase current, respectively, and  $R_L$  is DC load.

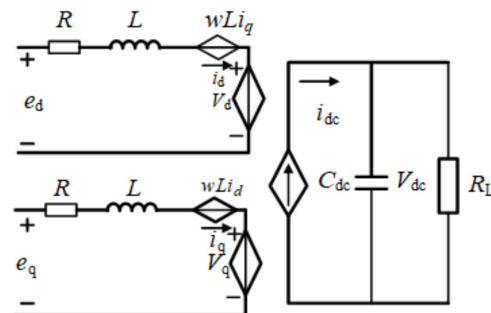


Figure 7. Equivalent model of PWM rectifier.

Generally, distributed generation units are equivalent to an AC voltage source. The power of CPLs is  $P$ . The AC voltage source's d- and q-axes are  $e_d$  and 0. The DC–DC converter of battery adopts a voltage and current double-closed-loop control. The battery functions in the same way as a controlled power source when the batteries are in the process of discharging, and the discharging power is  $P_b$ .  $R_a$  is the AC resistive load.  $L_s$  and  $C_s$  are filter inductance and capacitance, respectively, and  $R_s$  is the line-equivalent resistance. DC bus voltage is denoted by  $v_{dc}$ , and DC capacitance is denoted by  $C_{dc}$ . Figure 8 shows the equivalent model of AC/DC Hybrid Microgrids with the battery in discharging mode.

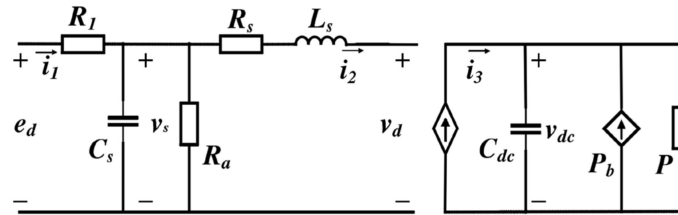


Figure 8. The equivalent model of AC/DC Hybrid Microgrids in discharging.

Similarly, when in charging mode, the battery absorbs power and is equivalent to resistance  $R$ . The power of  $R$  is the battery charging power  $P_{ch}$ . The equivalent model when the battery is in charging mode is shown in Figure 9.

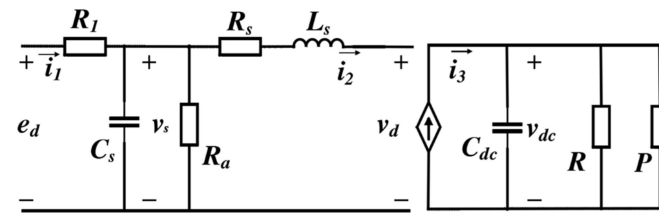


Figure 9. The equivalent model of AC/DC Hybrid Microgrids in charging.

To sum up, the equivalent models of microgrids are shown in Figures 8 and 9. The current of the DC-equivalent controlled current source is controlled by  $v_d$ . At the same time, the relationship between  $i_3$  and  $v_d$  is:

$$i_3 = \frac{3v_d i_2}{2v_{dc}} \tag{2}$$

According to Figure 8 and (2), the steady-state equilibrium point A ( $V_s, V_{dc}, i_2$ ) of microgrids in discharging mode is obtained, and shown as:

$$\begin{cases} i_3 v_{dc} + P_b = P \\ v_s - v_d - i_2 R_s = 0 \\ 2v_{dc} i_3 = 3v_d i_2 \\ i_1 = \frac{v_s}{R_a} + i_2 \\ e_d = i_1 R_1 + v_s \end{cases} \tag{3}$$

Similarly, based on Figure 9 and (2),  $P_{ch}$  is the charging power. The steady-state equilibrium point B ( $V_s, V_{dc}, i_2$ ) of microgrids in charging mode is shown as:

$$\begin{cases} i_1 = \frac{v_s}{R_a} + i_2 \\ e_d = i_1 R_1 + v_s \\ 2v_{dc} i_3 = 3v_d i_2 \\ i_3 v_{dc} = P + P_{ch} \\ v_s - v_d - i_2 R_s = 0 \end{cases} \tag{4}$$

### 3. Large Signal Stability Analysis of AC/DC Hybrid Microgrids

#### 3.1. Large Signal Models and Stability Criteria When Battery Is in Discharging Mode

Brayton and Moser first presented the mixed potential method in 1964, which has been widely used to study the stability of large signals in nonlinear systems [35–38]. According to the equivalent model of microgrids in discharging mode in Figure 8, the state variables are DC bus voltage  $v_{dc}$ , AC side inductor current  $i_2$ , and AC bus voltage  $v_s$ . A large signal nonlinear model was built as per mixed potential theory.

$$P(i, v) = e_d i_1 - \frac{1}{2} i_1^2 R_1 - \frac{1}{2} i_2^2 R_s - v_d i_2 - \int_0^{v_{dc}} i_3 dv + \int_0^{v_{dc}} \frac{P}{v} dv + \frac{v_s^2}{2R_a} - \int_0^{v_{dc}} \frac{P_b}{v} dv + v_s i_2 - v_s i_1 \tag{5}$$

Then, the current potential function is achieved and shown as:

$$A(i) = -(e_d i_1 - \frac{1}{2} i_1^2 R_1 - \frac{1}{2} i_2^2 R_s - v_d i_2) \tag{6}$$

The voltage potential function is:

$$B(v) = - \int_0^{v_{dc}} i_3 dv + \int_0^{v_{dc}} \frac{P}{v} dv + \frac{v_s^2}{2R_a} - \int_0^{v_{dc}} \frac{P_b}{v} dv + v_s i_2 - v_s i_1 \tag{7}$$

According to (6) and (7), the following formulas are obtained:

$$L^{-1/2} A(ii) L^{-1/2} = \frac{R_s}{L_s} \tag{8}$$

$$C^{-1/2} B(vv) C^{-1/2} = \begin{bmatrix} \frac{1}{C_s R_a} & 0 \\ 0 & \frac{P_b}{C_{dc} v_{dc}^2} - \frac{P}{C_{dc} v_{dc}^2} \end{bmatrix} \tag{9}$$

In accordance with the mixed potential function’s third stability theorem, the minimal eigenvalues of the matrices  $L^{-1/2} A_{ii}(i) L^{-1/2}$  and  $C^{-1/2} B_{uu}(u) C^{-1/2}$  are  $\mu_1$  and  $\mu_2$ , respectively. According to (8) and (9),  $\mu_1$  and  $\mu_2$  are shown as:

$$\mu_1 = \frac{R_s}{L_s} \quad \mu_2 = \min \left\{ \frac{1}{C_s R_a}, \frac{1}{C_{dc}} \left( \frac{P_b - P}{v_{dc}^2} \right) \right\} \tag{10}$$

To guarantee large signal stability,  $\mu_1 + \mu_2$  is required to be more than zero. Consequently, the large signal stability criteria of microgrids in discharging mode are derived as follows:

$$\frac{R_s}{L_s} + \min \left\{ \frac{1}{C_s R_a}, \frac{1}{C_{dc}} \left( \frac{P_b - P}{v_{dc}^2} \right) \right\} > 0 \tag{11}$$

The proposed criteria in (11) indicates that when the battery is in discharging mode, large signal stability of microgrids is related to the battery’s discharging power  $P_b$ , the DC voltage  $V_{dc}$ , the CPL power  $P$ , the AC resistive load  $R_a$ , the DC capacitor  $C_{dc}$ , the AC inductor  $L_s$  and the AC capacitor  $C_s$ .

#### 3.2. Large Signal Models and Stability Criteria When Battery in Charging Mode

Similarly, based on the equivalent model of AC/DC Hybrid Microgrids when the battery is in charging mode as shown in Figure 9, we obtained the following large signal nonlinear model:

$$P(i, v) = e_d i_1 - \frac{1}{2} i_1^2 R_1 - \frac{1}{2} i_2^2 R_s - v_d i_2 - \int_0^{v_{dc}} i_3 dv + \int_0^{v_{dc}} \frac{P}{v} dv + \frac{v_s^2}{2R_a} + \frac{v_{dc}^2}{2R} + v_s i_2 - v_s i_1 \tag{12}$$

The current potential function is:

$$A(i) = -(e_d i_1 - \frac{1}{2} i_1^2 R_1 - \frac{1}{2} i_2^2 R_s - v_d i_2) \tag{13}$$

The voltage potential function is:

$$B(v) = - \int_0^{v_{dc}} i_3 dv + \int_0^{v_{dc}} \frac{P}{v} dv + \frac{v_s^2}{2R_a} + \frac{v_{dc}^2}{2R} + v_s i_2 - v_s i_1 \tag{14}$$

Large signal stability criteria of Microgrids when the battery is in charging mode is:

$$\frac{R_s}{L_s} + \min \left\{ \frac{1}{C_s R_a}, \frac{1}{C_{dc}} \left( \frac{-P_{ch} - P}{v_{dc}^2} \right) \right\} > 0 \tag{15}$$

The criteria in (15) show that when the battery is in charging mode, large signal stability criteria are related to the DC voltage  $V_{dc}$ , the CPL power  $P$ , the AC resistive load  $R_a$ , the DC capacitor  $C_{dc}$ , the AC inductor  $L_s$ , the AC capacitor  $C_s$ , and the charging power  $P_{ch}$  of batteries.  $P_{ch}$  is the power of the equivalent battery resistor  $R$ .

#### 4. Three-Dimensional RAS

##### 4.1. Three-Dimensional RAS When Battery Is in Discharging Mode

Based on (5), the Lyapunov function of microgrids when the battery is in discharging mode was calculated and shown as [37,38]:

$$P^*(i, v) = \frac{\mu_1 - \mu_2}{2} P(i, v) + \frac{1}{2L_s} (-i_2 R_s + v_s - v_d)^2 + \frac{1}{2C_s} \left( i_2 + \frac{v_s}{R_a} - i_1 \right)^2 + \frac{1}{2C_{dc}} \left( -i_3 - \frac{P_b}{v_{dc}} + \frac{P}{v_{dc}} \right)^2 \tag{16}$$

The first-order time derivative of the Lyapunov function is:

$$\begin{aligned} \frac{dP^*(i, v)}{dt} &= \frac{\mu_1 - \mu_2}{2} \frac{dP(i, v)}{dt} + \frac{1}{L_s} \left( \frac{\partial P}{\partial i_2} \right) \left( -\frac{di_2}{dt} R_s + \frac{dv_s}{dt} \right) + \frac{1}{C_s} \left( \frac{\partial P}{\partial v_s} \right) \left( \frac{di_2}{dt} + \frac{1}{R_a} \frac{dv_s}{dt} \right) \\ &+ \frac{1}{C_{dc}} \left( \frac{\partial P}{\partial v_{dc}} \right) \left( \frac{P_b}{v_{dc}^2} \frac{dv_{dc}}{dt} - \frac{P}{v_{dc}^2} \frac{dv_{dc}}{dt} \right) \end{aligned} \tag{17}$$

In (17), it is satisfied that:

$$\begin{aligned} \frac{di_2}{dt} &= \frac{1}{L_s} \left( \frac{\partial P}{\partial i_2} \right) = \frac{1}{L_s} (-i_2 R_s + v_s - v_d) \\ \frac{dv_s}{dt} &= -\frac{1}{C_s} \left( \frac{\partial P}{\partial v_s} \right) = -\frac{1}{C_s} \left( i_2 + \frac{v_s}{R_a} - i_1 \right) \\ \frac{dv_{dc}}{dt} &= -\frac{1}{C_{dc}} \left( \frac{\partial P}{\partial v_{dc}} \right) = -\frac{1}{C_{dc}} \left( -i_3 - \frac{P_b}{v_{dc}} + \frac{P}{v_{dc}} \right) \end{aligned} \tag{18}$$

It is necessary to determine whether the Lyapunov function.

$P^*(i, v)$  is positive definite, and at the same time determine whether the first-order derivative of the Lyapunov function with respect to time  $dP^*(i, v)/dt$  is negative definite. If the Lyapunov function is positive definite, at the same time, the first order derivative of it is negative definite, and the RAS exists.

Based on (16) and (17), combined with the LaSalle invariant principle, 3D RAS of microgrids when the battery is in discharging mode is:

$$RAS = \left\{ (v_s, v_{dc}, i_2) : P^*(v_s, v_{dc}, i_2) \leq \min_{i_2, v_s} P^*(v_s, v_{dc, min}, i_2) \right\} \tag{19}$$

##### 4.2. Three-Dimensional RAS When Battery Is in Charging Mode

Similarly, based on (12), the Lyapunov function of microgrids when the battery is in charging mode is calculated and shown as:

$$P^*(i, v) = \frac{\mu_1 - \mu_2}{2} P(i, v) + \frac{1}{2L_s} (-i_2 R_s + v_s - v_d)^2 + \frac{1}{2C_s} \left( i_2 + \frac{v_s}{R_a} - i_1 \right)^2 + \frac{1}{2C_{dc}} \left( -i_3 + \frac{P_{ch}}{v_{dc}} + \frac{P}{v_{dc}} \right)^2 \tag{20}$$

The first-order time derivative of the Lyapunov function is:

$$\begin{aligned} \frac{dP^*(i,v)}{dt} = & \frac{\mu_1 - \mu_2}{2} \frac{dP(i,v)}{dt} + \frac{1}{L_s} \left( \frac{\partial P}{\partial i_2} \right) \left( -\frac{di_2}{dt} R_s + \frac{dv_s}{dt} \right) + \frac{1}{C_s} \left( \frac{\partial P}{\partial v_s} \right) \left( \frac{di_2}{dt} + \frac{1}{R_a} \frac{dv_s}{dt} \right) \\ & + \frac{1}{C_{dc}} \left( \frac{\partial P}{\partial v_{dc}} \right) \left( -\frac{P_{ch}}{v_{dc}^2} \frac{dv_{dc}}{dt} - \frac{P}{v_{dc}^2} \frac{dv_{dc}}{dt} \right) \end{aligned} \quad (21)$$

In (21), it is satisfied that:

$$\begin{aligned} \frac{di_2}{dt} = & \frac{1}{L_s} \left( \frac{\partial P}{\partial i_2} \right) = \frac{1}{L_s} (-i_2 R_s + v_s - v_d) \\ \frac{dv_s}{dt} = & -\frac{1}{C_s} \left( \frac{\partial P}{\partial v_s} \right) = -\frac{1}{C_s} \left( i_2 + \frac{v_s}{R_a} - i_1 \right) \\ \frac{dv_{dc}}{dt} = & -\frac{1}{C_{dc}} \left( \frac{\partial P}{\partial v_{dc}} \right) = -\frac{1}{C_{dc}} \left( -i_3 + \frac{P_{ch}}{v_{dc}} + \frac{P}{v_{dc}} \right) \end{aligned} \quad (22)$$

Similarly, 3D RAS of AC/DC Hybrid Microgrids when the battery is in charging mode is also shown as (19).

### 5. Experimental Verification of Large Signal Stability Criteria and 3D RAS

According to Figure 1, to confirm the accuracy of the suggested large signal stability criteria in (11) and (12), an experimental platform of AC/DC hybrid microgrids was constructed (15), and also to verify 3D RAS in (19). The experimental platform is shown in Figure 10, and is composed of an AC voltage source, DC–DC bidirectional converter, DC–AC bidirectional converter, AC resistive load, CPLs and batteries.

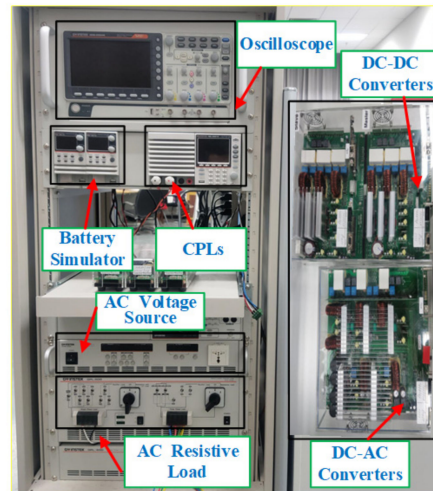


Figure 10. AC/DC Hybrid Microgrid experimental platform.

Large disturbances are introduced by power variations of CPLs. Table 1 displays the experimental platform’s parameters.

Table 1. Experimental platform parameters of microgrids.

Parameters	Value
AC inductor ( $L_s$ )	1000 $\mu$ H
AC filter capacitor ( $C_s$ )	680 $\mu$ F
DC capacitor ( $C_{dc}$ )	200 $\mu$ F
AC voltage source	20 V
$P_b$ batteries discharging power	20 W

5.1. Experimental Verification of 3D RAS and Large Signal Stability Criteria When the Battery Is in Discharging Mode

When the battery is in discharging mode, at the same time, the initial power of CPLs is 40 W. Based on Table 1 and (3), the initial steady-state equilibrium point of system is (19.92 V, 60 V, 0.67 A). Furthermore, according to (11), the large signal stability criteria is shown as:

$$\frac{R_s}{L_s} + \frac{P_b}{C_{dc}v_{dc}^2} - \frac{P}{C_{dc}v_{dc}^2} > 0 \tag{23}$$

From (23), the power of CPL must satisfy the following conditions in order to ensure large signal stability:

$$P < 92 \text{ W} \tag{24}$$

Two group experiments were performed: Group A, the power variation of CPLs from 40 W to 80 W, and Group B, the power variation of CPLs from 40 W to 100 W. Obviously, Group A’s parameters met the condition (24), while Group B’s parameters did not (24).

Firstly, Group A was adopted. When the power of CPLs increased from 40 W to 80 W, the new steady-state equilibrium point was (19.85 V, 60 V, 2.04 A). According to (16), the Lyapunov function is:

$$P^*(i, v) = \frac{1}{2} \left( \frac{R_s}{L_s} - \frac{P_b - P}{C_{dc}v_{dc}^2} \right) + \frac{1}{2L_s} (-i_2R_s + v_s - v_d)^2 + \frac{1}{2C_s} \left( i_2 + \frac{v_s}{R_a} - i_1 \right)^2 + \frac{1}{2C_{dc}} \left( -i_3 - \frac{P_b}{v_{dc}} + \frac{P}{v_{dc}} \right)^2 \tag{25}$$

The slice function of Matlab was used to color the Lyapunov function, and values are reflected by the different colors. Figure 11 is the four-dimensional Lyapunov function of microgrids when the battery is in discharging mode.

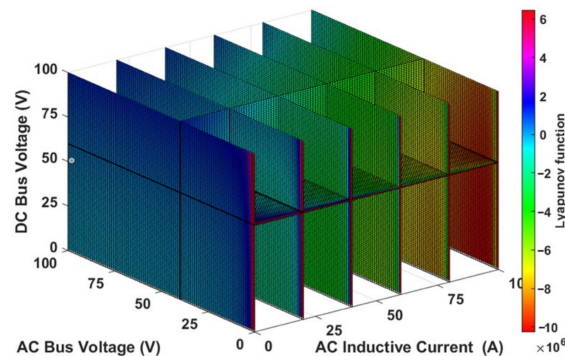


Figure 11. Four-dimensional graph of Lyapunov function of microgrids with the battery in discharging mode.

In Figure 11, the positive definite Lyapunov function exists. According to (17), the first-order time derivative of the Lyapunov function is:

$$\begin{aligned} \frac{dP^*(i,v)}{dt} = & \frac{1}{2} \left( \frac{R_s}{L_s} - \frac{P_b - P}{C_{dc}v_{dc}^2} \right) \frac{dP(i,v)}{dt} + \frac{1}{L_s} \left( \frac{\partial P}{\partial i_2} \right) \left( -\frac{di_2}{dt} R_s + \frac{dv_s}{dt} \right) + \frac{1}{C_s} \left( \frac{\partial P}{\partial v_s} \right) \left( \frac{di_2}{dt} + \frac{1}{R_a} \frac{dv_s}{dt} \right) \\ & + \frac{1}{C_{dc}} \left( \frac{\partial P}{\partial v_{dc}} \right) \left( \frac{P_b}{v_{dc}^2} \frac{dv_{dc}}{dt} - \frac{P}{v_{dc}^2} \frac{dv_{dc}}{dt} \right) \end{aligned} \tag{26}$$

The slice function of Matlab was also used to color  $dP^*(i,v)/dt$ , as shown in Figure 12. Obviously, negative definite  $dP^*(i,v)/dt$  exists.

Figures 11 and 12 indicate that 3D RAS exists. Based on (19), the 3D RAS of Hybrid Microgrids with the battery in discharging mode (CPLs power was 40 W) was derived and shown in Figure 13. The steady-state equilibrium point when CPL power was 40 W is also marked with \*. It can be observed from Figure 13 that the equilibrium point is in the 3D RAS of microgrids.

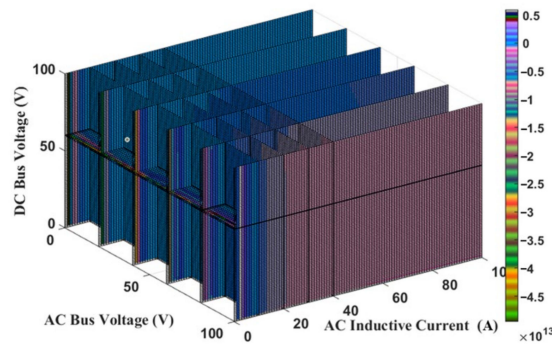


**Figure 12.** Four-dimensional graph of the first derivative of Lyapunov function with respect to time of microgrids with the battery in discharging mode.

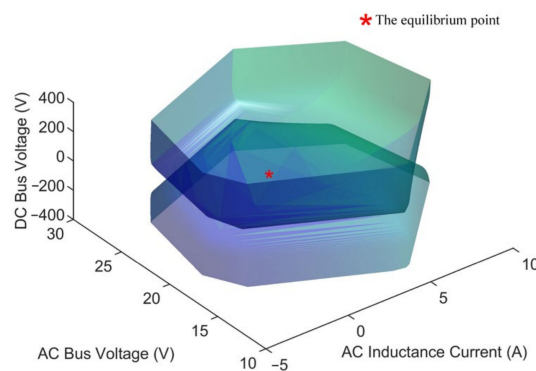


**Figure 13.** The 3D RAS of microgrids with the battery in discharging mode (CPLs power is 40 W).

Similarly, when the CPLs power was increased to 80 W, the new 3D RAS and new equilibrium point of microgrids with the battery in discharging mode were both derived and shown in Figure 14. It is definite that the 3D RAS of 40 W is larger than the 3D RAS of 80 W, and both steady-state equilibrium points are in 3D RAS. Comparisons indicate that as the power of CPLs increases, the negative impedance characteristic becomes stronger, and the stability margin of microgrids with the battery in discharging mode is reduced. The positions of two steady-state equilibrium points show that microgrids would eventually reach the new equilibrium point. When Group A is applied, the system gained large signal stability.

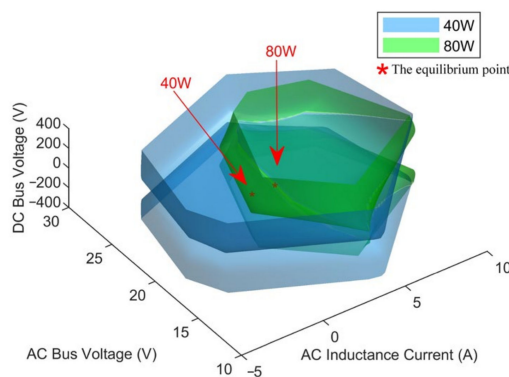


**Figure 14.** The 3D RAS of microgrids with the battery in discharging mode (CPL power is 40 W and 80 W).

As Group A is utilized in the AC/DC Hybrid Microgrid experimental platform, AC and DC bus voltage waveforms when CPLs power varied from 40 W to 80 W are shown in Figure 15. When the power of CPLs was 40 W, the AC bus voltage is 20 V and the DC bus voltage is 60 V. When the CPL’s power rose from 40 W to 80 W, nevertheless, the AC bus

voltage was always stable at 20 V, and eventually, after a brief decrease, the DC bus voltage stabilized at 60 V. The AC and DC bus voltage were both stable with large disturbances, and the experimental results coincided with Figure 14.

Figure 15 illustrates that if parameters satisfy (24), AC/DC Hybrid Microgrids with the battery in discharging mode could achieve large signal stability. Unfortunately, methods of improving stability are not mentioned in the proposed large signal stability criterion. Furthermore, the 3D RAS in Figure 14 clearly provides the stability margins of AC/DC Hybrid Microgrids with the battery in discharging mode. Consequently, the 3D RAS method is very popular for achieving sufficiently large stability margins, and expands the application of stability criterion in (24). The 3D RAS method, combined with large signal stability criteria, could improve system stability by optimizing stability margins.

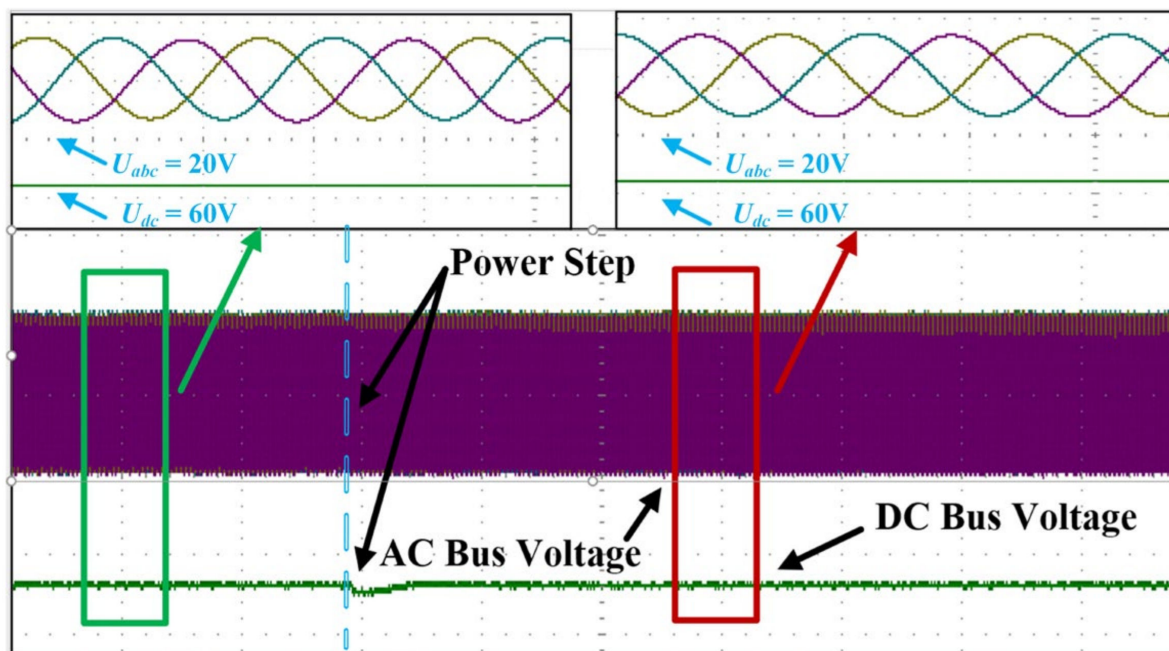


**Figure 15.** AC and DC bus voltage waveforms of microgrids when battery is in discharging mode (CPL power varied from 40 W to 80 W).

Next, Group B was adopted. When the power of CPLs increased from 40 W to 100 W, the new steady-state equilibrium point was (19.81 V, 60 V, 2.73 A), and the 3D RAS of AC/DC Hybrid Microgrids with the battery in discharging mode was also derived and shown in Figure 16. It is obvious that the 3D RAS of 40 W is larger than the 3D RAS of 100 W. The initial steady-state equilibrium point was within the 3D RAS of 40 W; unfortunately, the new equilibrium point was outside the 3D RAS of 100 W. Consequently, microgrids in discharging mode working at the initial equilibrium point would not reach a new equilibrium point. The system could not guarantee stable operation when Group B was utilized.

As Group B is utilized in the microgrid experimental platform, at the same time, Figure 17 shows AC and DC bus voltage waveforms for CPLs from 40 W to 100 W. When the power of CPLs was 40 W, AC and DC bus voltages were 20 V and 60 V, respectively. However, when the CPL power increased from 40 W to 100 W, DC bus voltage dropped from 60 V to 49.6 V and AC bus voltage decreased from 20 V to 18.5 V. Figure 17 indicates that the AC and DC bus voltage are not stable when large disturbances occur, and the experimental results coincide with Figure 16.

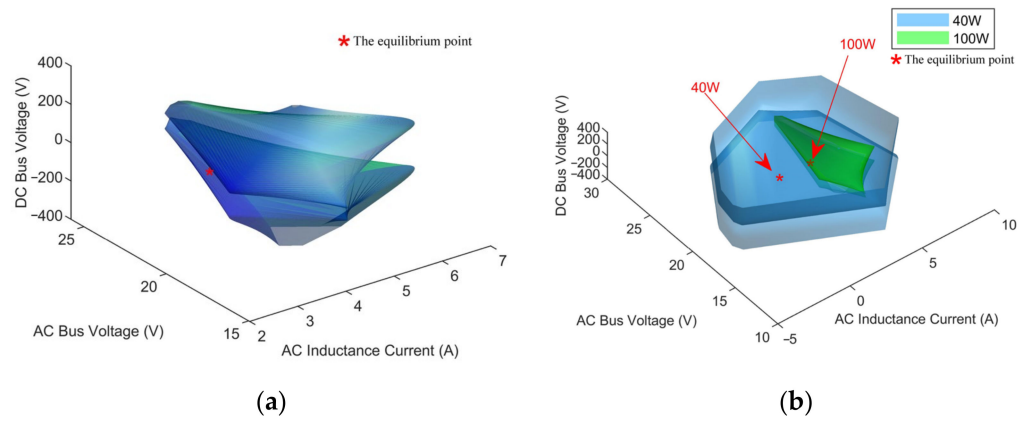


**Figure 16.** (a). The 3D RAS of microgrids with the battery in discharging mode (CPL power was 100 W). (b). The 3D RAS of microgrids with the battery in discharging mode (CPL power was 40 W and 100 W).

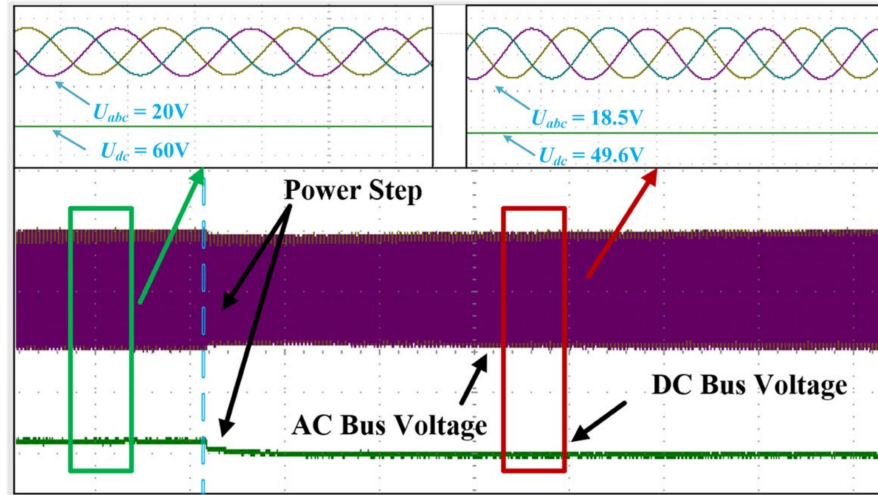


**Figure 17.** AC and DC bus voltage waveforms of microgrids with the battery in discharging mode (CPL power increased from 40 W and 100 W).

Figure 17 shows that, if parameters do not satisfy (24), microgrids with a battery in discharging mode cannot achieve large signal stability. Figure 16 clearly provides relationships between steady-state equilibrium points and 3D RAS; if the new steady-state equilibrium point is outside the new 3D RAS, the system cannot guarantee large signal stability. Consequently, the 3D RAS method is quite applicable to analyzing system stability.

Figures 14–17 validate the large signal stability criteria (24). Figures 14 and 16 show that the 3D RAS method can analyze the system stability and simultaneously improve system stability by optimizing stability margins.

*5.2. Experimental Verification of 3D RAS and Large Signal Stability Criterion When the Battery Is in Charging Mode*

The initial power of CPLs was 20 W when the battery was working in charging mode. Similarly, based on Table 1 and (4), the initial equilibrium point of microgrids was (19.88 V, 60 V, 1.35 A). Furthermore, according to (15), large signal stability was obtained and represented as:

$$\frac{R_s}{L_s} + \frac{1}{C_{dc}} \left( \frac{-P_{ch} - P}{v_{dc}^2} \right) > 0 \tag{27}$$

From (27), the power of CPL must satisfy the following conditions in order to ensure large signal stability:

$$P < 54 \text{ W} \tag{28}$$

Two group experiments were arranged. Group C represents the power variation of CPLs from 20 W to 45 W, and Group D represents the power variation of CPLs from 20 W to 60 W. Obviously, Group C’s parameters meet the condition (28), while Group D’s parameters do not (28).

Firstly, Group C was adopted. When the power of CPLs increased from 20 W to 45 W, the new steady-state equilibrium point was (19.84 V, 60 V, 2.14 A).

Based on (19), the 3D RAS of microgrids with the battery in charging mode (CPLs power is 20 W) was derived and shown in Figure 18. The steady-state equilibrium point when CPL power was 20 W was also marked with \*. It can be observed from Figure 18 that the equilibrium point was inside the 3D RAS of microgrids.

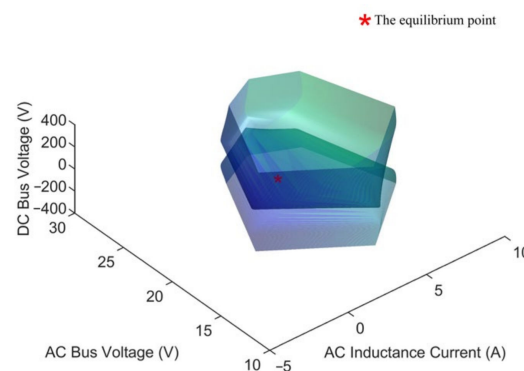


Figure 18. The 3D RAS of microgrids with the battery in charging mode (CPL power was 20 W).

Similarly, when the CPLs power was increased to 45 W, the new 3D RAS and new steady-state equilibrium point of microgrids when the battery is in charging mode were both derived and shown in Figure 19. It is definite that the 3D RAS of 20 W was larger than the 3D RAS of 45 W. As the power of CPLs increases, the negative impedance characteristic becomes stronger, and the system stability margin is significantly reduced. Because both equilibrium points are in 3D RAS, AC/DC Hybrid Microgrids would eventually reach the new equilibrium point. When Group C is used, the system obtained large signal stability.

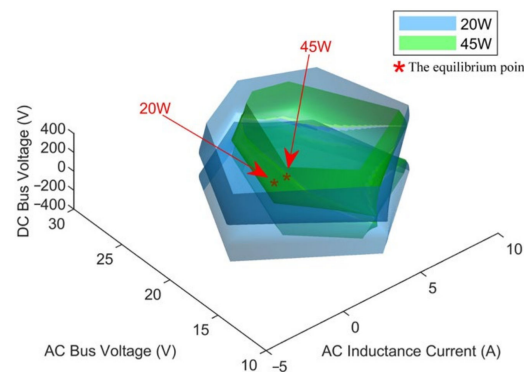


Figure 19. The 3D RAS of microgrids with the battery in charging mode (CPL power was 20 W and 45 W).

As Group C was utilized in the AC/DC Hybrid Microgrids experimental platform, at the same time, the AC and DC bus voltage waveforms when CPL power varied from 20 W to 45 W are shown in Figure 20. The AC bus voltage was 20 V and the DC bus voltage was 60 V when the power of CPLs was 20 W. When the CPL power increased from 20 W to 45 W, the AC bus voltage was always stable at 20 V, and eventually, after a brief decrease, the DC bus voltage stabilized at 60 V. The AC and DC bus voltage were both stable when large disturbances occurred, and the experimental results coincide with Figure 19.

Figure 20 illustrates that if parameters satisfy (28), microgrids with the battery in charging mode could achieve large signal stability. Figure 19 shows that the 3D RAS method, combined with large signal stability criterion, could optimize stability margins and also improve system stability.

Then, Group D was adopted. When the power of CPLs increased from 20 W to 60 W, the new steady-state equilibrium point was (19.82 V, 60 V, 2.66 A), and the 3D RAS of microgrids with the battery in charging mode was derived and shown in Figure 21. It is obvious that the 3D RAS of 20 W was larger than the 3D RAS of 60 W. However, both steady-state equilibrium points were outside the 3D RAS of 60 W. Consequently, AC/DC Hybrid Microgrids, when the battery is in charging mode, would not reach the new equilibrium point from the initial equilibrium point. The system could not guarantee stable operation when Group D was utilized.

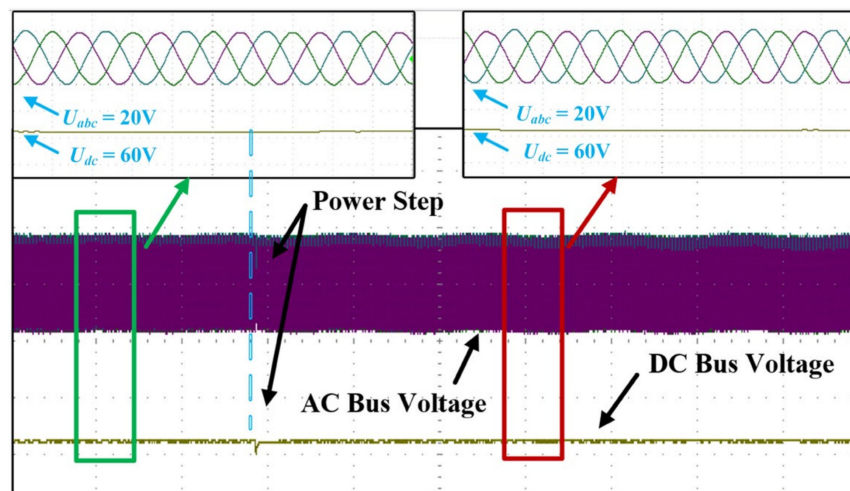


Figure 20. AC and DC bus voltage waveforms of microgrids when the battery is in charging mode (CPL power varied from 20 W to 45 W).

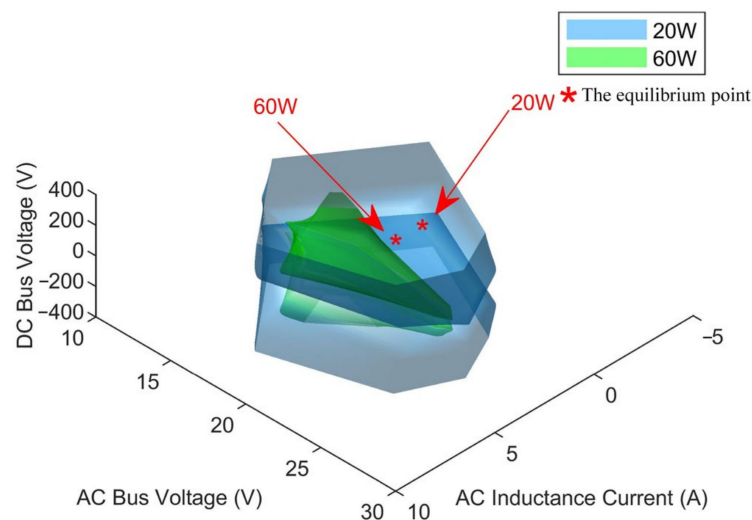


Figure 21. The 3D RAS of microgrids with the battery in charging mode (CPL power was 20 W and 60 W).

As Group D was used in the AC/DC Hybrid Microgrids experimental platform, AC and DC bus voltage waveforms when CPLs power varies from 20W to 60W are shown in Figure 22. When the power of CPLs is 20 W, voltage is 20 V for the AC bus and 60 V for the DC bus, respectively. Unfortunately, when the CPL power increases from 20 W to 60 W, DC bus voltage drops from 60 V to 40.5 V, and simultaneously, AC bus voltage decreases from

20 V to 18.2 V. Figure 22 indicates the AC and DC bus voltage are not stable during large disturbances, and the experimental results coincide with Figure 21.

Figure 22 shows if parameters do not satisfy (28), Microgrids when battery in charging mode could not achieve large signal stability. Figure 21 provides relationships between steady-state equilibrium points and 3D RAS, if the new steady-state equilibrium point is outside the new 3D RAS, the system would not guarantee large signal stability. Consequently, 3D RAS method is very useful to analyze the system stability.

Figures 19–22 validate the large signal stability criteria (28). Figures 19 and 21 show that the 3D RAS is capable of describing the stability and instability of the system and of enhancing system stability by optimizing the stability margin.

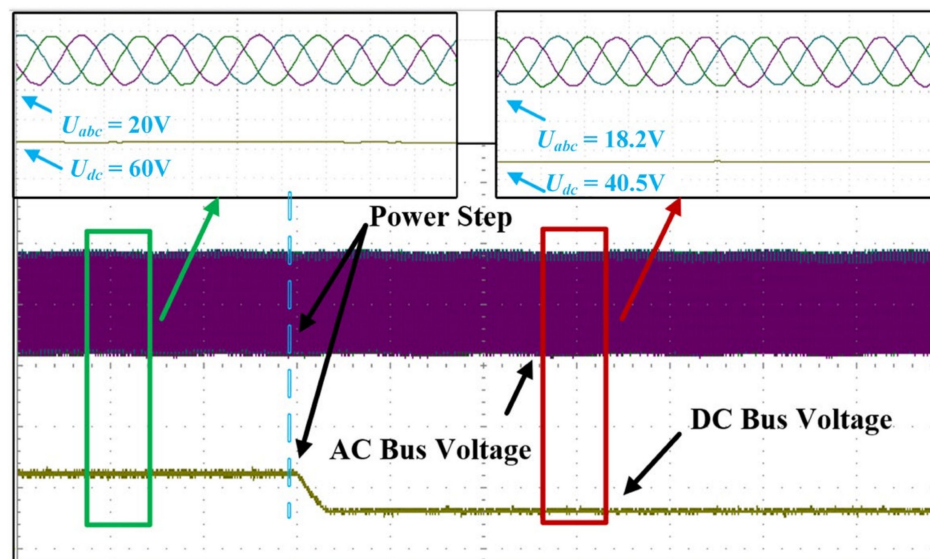


**Figure 22.** AC and DC bus voltage waveforms of microgrids when the battery is in charging mode (CPLs power varies from 20 W to 60 W).

### 5.3. Important Parameters to Increase Stability Margins

The size of AC/DC Hybrid Microgrids 3D RAS are significantly influenced by the charging and discharging power of the battery, DC bus capacitor  $C_{dc}$ , AC inductance  $L_s$  and AC capacitor  $C_s$ . Stability margins could be increased by optimizing these parameters.

To illustrate if these parameters have positive or negative characteristics in relation to 3D RAS. Compare the 3D RAS when one parameter changes while the other system parameters remain constant.

Firstly, the influence on 3D RAS from battery discharging power  $P_b$  was analyzed. When discharging powers were 20 W, 30 W and 40 W, the 3D RAS were derived, respectively, and shown in Figure 23. It is observed from Figure 23 that as the battery discharging power increases, the 3D RAS of AC/DC Hybrid Microgrids also significantly increases.

Then, the influence on 3D RAS from battery charging power  $P_{ch}$  was considered. When charging powers are 45 W, 60 W and 75 W, the 3D RAS are shown in Figure 24. It is confirmed that as the battery charging power increases, the 3D RAS of AC/DC Hybrid Microgrids decreases. Similarly, it is confirmed that if the loads consuming power become bigger, the 3D RAS of AC/DC Hybrid Microgrids becomes smaller.

The influence on 3D RAS of the DC bus capacitor  $C_{dc}$  was analyzed. When DC bus capacitors were 200  $\mu\text{F}$ , 400  $\mu\text{F}$  and 600  $\mu\text{F}$ , the 3D RAS were derived, respectively, and shown in Figure 25. It is obvious that as the DC bus capacitors increase, the 3D RAS of AC/DC Hybrid Microgrids also increases.

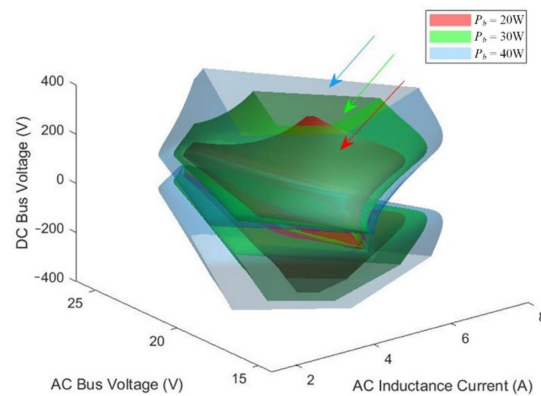


**Figure 23.** Different 3D RAS of microgrids when battery discharging powers are 20 W, 30 W and 40 W.

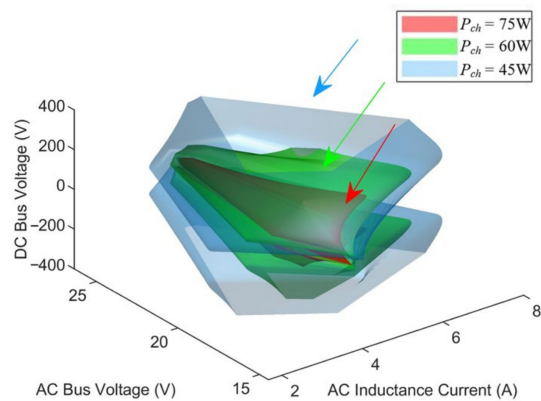


**Figure 24.** Different 3D RAS of microgrids when battery charging powers are 45 W, 60 W and 75 W.

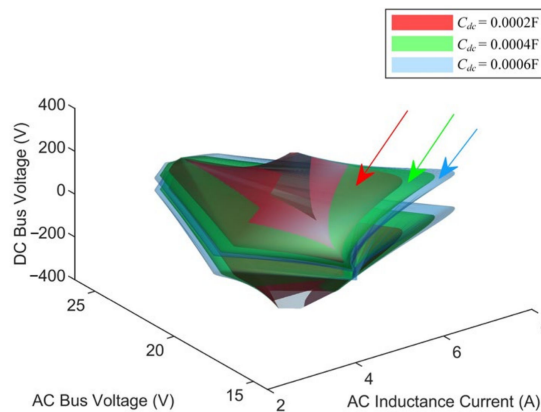


**Figure 25.** Different 3D RAS of microgrids when DC bus capacitors are 0.0002 F, 0.0004 F and 0.0006 F.

The influence on 3D RAS from AC capacitor  $C_s$  was considered. When AC capacitors were 680  $\mu\text{F}$ , 1000  $\mu\text{F}$  and 1500  $\mu\text{F}$ , the 3D RAS were as shown in Figure 26. It is confirmed that as the AC capacitor increases, the 3D RAS of AC/DC Hybrid Microgrids also increases.

In summary, in order to increase the stability margins and 3D RAS of islanded AC/DC Hybrid Microgrids, the DC bus capacitor and AC capacitor can be increased appropriately. Furthermore, the power also plays an important role in stability margins and 3D RAS. A larger battery discharging power increases 3D RAS, while smaller loads consuming power also lead to larger 3D RAS.

The 3D RAS method could clearly recognize the key parameters determining stability margins, and could also easily improve stability through parameter optimization.

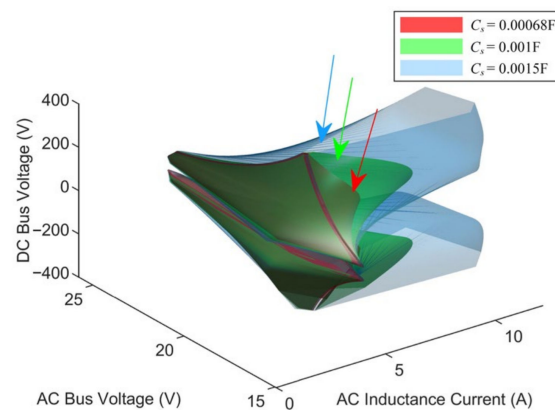


**Figure 26.** Different 3D RAS of microgrids when AC capacitors are 0.00068 F, 0.001 F and 0.0015 F.

## 6. Conclusions

This paper proposed large signal stability criteria combined with the 3D RAS method to guarantee islanded AC/DC Hybrid Microgrid stability during large disturbances. Firstly, equivalent nonlinear models in the dq rotating coordinate system were established. Then, large signal stability criteria were obtained based on mixed potential function. Lastly, Lyapunov functions were constructed, and the Lasalle invariance principle was adopted to obtain the 3D RAS of islanded AC/DC Hybrid Microgrids.

In particular, filtering parameters, CPL power, battery charging and discharging power, AC resistive loads, and DC bus voltage were all interpreted by the large signal stability criteria. Additionally, the derived 3D RAS was related to DC bus capacitor voltage, AC capacitor voltage and AC inductor current, and is extremely applicable for indicating the stability margins of complicated AC/DC Hybrid Microgrids.

The presented large signal stability criteria, combined with the 3D RAS method for islanded AC/DC Hybrid Microgrids, clearly provides important system parameters. To increase stability margins, increasing the capacitance of the DC bus capacitor and the AC capacitor, and increasing the discharging power of batteries are all very effective methods.

The large signal stability criteria, combined with the 3D RAS method for an islanded AC/DC Hybrid Microgrids system, not only provides a visual and intuitive opportunity for large-signal stability analysis, but also gives important stability design conditions for increasing large signal stability margins.

**Author Contributions:** Study design, literature search, manuscript writing, X.L.; graph production, data analysis, data processing, Z.Z.; supervision, data collection, J.S.; resources, review and editing, X.S.; translation, literature search, J.Z. All authors have read and agreed to the published version of the manuscript.

**Funding:** National Key R&D Program of China, Grant/Award Number: 2021YFE0103800; Beijing High-Level Innovation Team Building Plan, Grant/Award Number: IDHT20180502.

**Conflicts of Interest:** The authors declare no conflict of interest.

## References

1. Shafiullah, G.M.; Masola, T.; Samu, R.; Elavarasan, R.M.; Begum, S.; Subramania, U. Prospects of Hybrid Renewable Energy-Based Power System: A Case Study, Post Analysis of Chipendeke Micro-Hydro, Zimbabwe. *IEEE Access* **2021**, *9*, 73433–73452. [[CrossRef](#)]
2. Ullah, N.; Farooq, Z.; Sami, I.; Chowdhury, M.S.; Techato, K.; Alkhamash, H.I. Industrial Grade Adaptive Control Scheme for a Micro-Grid Integrated Dual Active Bridge Driven Battery Storage System. *IEEE Access* **2020**, *8*, 210435–210451. [[CrossRef](#)]
3. Lasseter, R.H. 2002 *IEEE Power Engineering Society Winter Meeting. Conference Proceedings*; IEEE: Piscataway, NJ, USA, 2002; Volume 1, pp. 305–308.
4. Loh, P.C.; Li, D.; Chai, Y.K.; Blaabjerg, F. Autonomous Operation of Hybrid Microgrid with AC and DC Subgrids. *IEEE Trans. Power Electron.* **2013**, *28*, 2214–2223. [[CrossRef](#)]
5. Mohamed, S.; Mokhtar, M.; Marei, M.I. A Control Strategy for Hybrid Islanded Microgrid. In Proceedings of the 2019 21st International Middle East Power Systems Conference (MEPCON), Cairo, Egypt, 17–19 December 2019; pp. 301–306.

6. Awad, H.; Bayoumi, E.H.E.; Soliman, H.M.; De Santis, M. Robust Tracker of Hybrid Microgrids by the Invariant Ellipsoid Set. *Electronics* **2021**, *10*, 1794. [[CrossRef](#)]
7. Kaushik, R.A.; Pindoriya, N.M. A hybrid AC-DC microgrid: Opportunities & key issues in implementation. In Proceedings of the 2014 International Conference on Green Computing Communication and Electrical Engineering (ICGCCEE), Coimbatore, India, 6–8 March 2014; pp. 1–6. [[CrossRef](#)]
8. Gao, F.; Wang, X.; Yang, P.; Kou, S.; Sun, M. Research and Simulation of Hybrid AC/DC Microgrid. In Proceedings of the 2020 4th International Conference on HVDC (HVDC), Xi'an, China, 9 November 2020; pp. 1276–1280.
9. Oureilidis, K.O.; Demoulias, C.S. An enhanced role for an energy storage system in a microgrid with converter-interfaced sources. *J. Eng.* **2014**, *2014*, 618–625. [[CrossRef](#)]
10. Gupta, A.; Doolla, S.; Chatterjee, K. Hybrid AC–DC Microgrid: Systematic evaluation of control strategies. *IEEE Trans. Smart Grid.* **2018**, *9*, 3830–3843. [[CrossRef](#)]
11. Sajid, A.; Sabzehgar, R.; Rasouli, M.; Fajri, P. Control of Interlinking Bidirectional Converter in AC/DC Hybrid Microgrid Operating in Stand-Alone Mode. In Proceedings of the 2019 IEEE Milan PowerTech, Milan, Italy, 23–27 June 2019.
12. Liu, X.; Zou, Y. Control Strategy of Super Capacitor-Battery Hybrid Energy Storage System Considering Constant Power Loads Characteristics. In Proceedings of the 2018 21st International Conference on Electrical Machines and Systems (ICEMS), Jeju, Republic of Korea, 7–10 October 2018; pp. 2095–2099.
13. Blanco-Contreras, B.; Meneses-Silva, J.; Mendoza-Araya, P.; Jiménez-Estévez, G. Effect of constant power load models on the stability of isolated Microgrids. In Proceedings of the 2019 IEEE CHILEAN Conference on Electrical Electronics Engineering Information and Communication Technologies (CHILECON), Valparaiso, Chile, 29–31 October 2019; pp. 1–6.
14. Liu, X.; Bian, Y. Large signal stability analysis of the DC microgrid with the storage system. In Proceedings of the 2017 20th International Conference on Electrical Machines and Systems (ICEMS), Sydney, Australia, 11–17 August 2017; pp. 1–5.
15. Liu, X.; Bian, Y.; Fan, S. Active stabilization control strategy for storage system paralleled with constant power loads. In Proceedings of the 2017 20th International Conference on Electrical Machines and Systems (ICEMS), Sydney, Australia, 11–17 August 2017; pp. 1–5.
16. Singh, S.V.; Shubhanga, K.N. Current injection modelling based large-signal analysis of a grid-connected solar photovoltaic power system. In Proceedings of the 2016 IEEE Annual India Conference (INDICON), Bangalore, India, 16–18 December 2016; pp. 1–6.
17. Huang, M.; Peng, Y.; Tse, C.K.; Liu, Y.; Sun, J.; Zha, X. Bifurcation and Large-Signal Stability Analysis of Three-Phase Voltage Source Converter Under Grid Voltage Dips. *IEEE Trans. Power Electron.* **2017**, *32*, 8868–8879. [[CrossRef](#)]
18. Mehmood, Y.; Aslam, J.; Ullah, N.; Chowdhury, M.S.; Techato, K.; Alzaed, A.N. Adaptive Robust Trajectory Tracking Control of Multiple Quad-Rotor UAVs with Parametric Uncertainties and Disturbances. *Sensors* **2021**, *21*, 2401. [[CrossRef](#)]
19. Kabalan, M.; Singh, P.; Niebur, D. Large Signal Lyapunov-Based Stability Studies in Microgrids: A Review. *IEEE Trans. Smart Grid* **2017**, *8*, 2287–2295. [[CrossRef](#)]
20. Marx, D.; Magne, P.; Nahid-Mobarakeh, B.; Pierfederici, S.; Davat, B. Large Signal Stability Analysis Tools in DC Power Systems With Constant Power Loads and Variable Power Loads—A Review. *IEEE Trans. Power Electron.* **2012**, *27*, 1773–1787. [[CrossRef](#)]
21. Xia, Y.; Lv, Z.; Wei, W.; He, H. Large-signal Stability Analysis and Control for Small-Scale AC Microgrids With Single Storage. *IEEE J. Emerg. Sel. Top. Power Electron.* **2021**, *10*, 4808–4820. [[CrossRef](#)]
22. Li, Z.; Pei, W.; Ye, H.; Kong, L. Large signal stability analysis for DC microgrid under droop control based on mixed potential theory. *J. Eng.* **2019**, *2019*, 1189–1193. [[CrossRef](#)]
23. Chen, D.; Ji, H.; Liu, Y.; Zha, X. Large Signal Modeling and Stability Analysis of Photovoltaic-Battery Hybrid Power System. In Proceedings of the 2018 IEEE Energy Conversion Congress and Exposition (ECCE), Portland, OR, USA, 23–27 September 2018; pp. 4168–4172.
24. Ndiwulu, G.W.; de Jaeger, E.; Lusala, A.K.; Matalatala, M. Large-Signal Stability Analysis for Islanded Microgrids Based on Inner Control Loops Approach. In Proceedings of the 2021 IEEE PES/IAS PowerAfrica, Virtual, 27 August 2021; pp. 1–5.
25. Rosado, S.; Burgos, R.; Wang, F.; Boroyevich, D. Large-Signal Stability Assessment of AC/DC Systems with Multi-Pulse Rectification and DC-Fed PWM Motor Drives. In Proceedings of the 2007 IEEE Power Electronics Specialists Conference, Orlando, FL, USA, 17–21 June 2007; pp. 2168–2173.
26. Chang, F.; Cui, X.; Wang, M.; Su, W. Potential-Based Large-Signal Stability Analysis in DC Power Grids With Multiple Constant Power Loads. *IEEE Open Access J. Power Energy* **2022**, *9*, 16–28. [[CrossRef](#)]
27. Zheng, H.; Yuan, X.; Cai, J.; Sun, P.; Zhou, L. Large-Signal Stability Analysis of DC Side of VSC-HVDC System Based on Estimation of Domain of Attraction. *IEEE Trans. Power Syst.* **2022**, *37*, 3630–3641. [[CrossRef](#)]
28. Liu, S.; Li, X.; Xia, M.; Qin, Q.; Liu, X. Takagi-Sugeno Multimodeling-Based Large Signal Stability Analysis of DC Microgrid Clusters. *IEEE Trans. Power Electron.* **2021**, *36*, 12670–12684. [[CrossRef](#)]
29. Kabalan, M.; Singh, P.; Niebur, D. Large signal stability analysis of a DC/AC droop controlled inverter connected to an infinite bus. In Proceedings of the 2015 North American Power Symposium (NAPS), Charlotte, NC, USA, 4–6 October 2015; pp. 1–6.
30. Kabalan, M.; Singh, P.; Niebur, D. A Design and Optimization Tool for Inverter-Based Microgrids Using Large-Signal Nonlinear Analysis. *IEEE Trans. Smart Grid* **2019**, *10*, 4566–4576. [[CrossRef](#)]
31. Andrade, F.; Kampouropoulos, K.; Romeral, L.; Vasquez, J.C.; Guerrero, J.M. Study of large-signal stability of an inverter-based generator using a Lyapunov function. In Proceedings of the IECON 2014 40th Annual Conference of the IEEE Industrial Electronics Society, Dallas, TX, USA, 29 October 2014; pp. 1840–1846.

32. Griffo, A.; Wang, J.; Howe, D. Large signal stability analysis of DC power systems with constant power loads. In Proceedings of the 2008 IEEE Vehicle Power and Propulsion Conference, Harbin, China, 3–5 September 2008; pp. 1–6.
33. Du, W.; Zhang, J.; Zhang, Y.; Qian, Z. Stability Criterion for Cascaded System With Constant Power Load. *IEEE Trans. Power Electron.* **2013**, *28*, 1843–1851. [[CrossRef](#)]
34. Belkhat, M.; Cooley, R.; Witulski, A. Large signal stability criteria for distributed systems with constant power loads. In Proceedings of the PESC '95-Power Electronics Specialist Conference, Atlanta, GA, USA, 6 August 2002.
35. Weiss, L.; Mathis, W.; Trajkovic, L. A generalization of Brayton-Moser's mixed potential function. *IEEE Trans. Circuits Syst. I Fundam. Theory Appl.* **1998**, *45*, 423–427. [[CrossRef](#)]
36. Guopeng, Z.; Xinwei, Z. Power requirement and control characteristics of energy storage equipment in a microgrid operating in island mode. *J. Eng.* **2017**, *2017*, 734–739. [[CrossRef](#)]
37. Brayton, R.K.; Moser, J.K. A theory of nonlinear networks I. *Quart. Appl. Math.* **1964**, *22*, 1–33. [[CrossRef](#)]
38. Brayton, R.K.; Moser, J.K. A theory of nonlinear networks II. *Quart. Appl. Math.* **1964**, *22*, 81–104. [[CrossRef](#)]